

Liquid Metal-Skinned Zn Powder Anodes Enabled by Capillary Suspension

Hyunseo Kang,^{||} Seung-Hyeok Kim,^{||} David B. Ahn, Xiao Wang, Zhong-Shuai Wu,^{*} and Sang-Young Lee^{*}



Cite This: *ACS Energy Lett.* 2024, 9, 2816–2825



Read Online

ACCESS |



Metrics & More

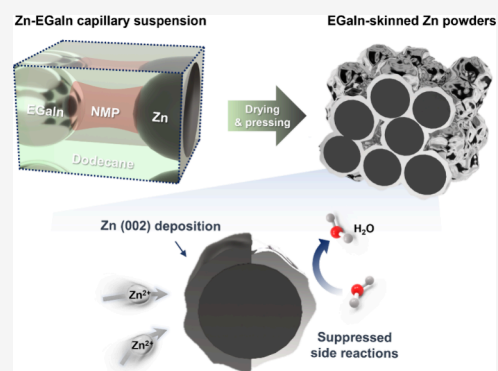


Article Recommendations



Supporting Information

ABSTRACT: Zinc (Zn) powder-based anodes have garnered considerable attention as viable alternatives to their conventional Zn foil-based counterparts. However, challenges arising from undesirable interfacial side reactions and dendritic Zn growth hinder their practical implementation. Here, we present a class of liquid metal-skinned Zn (LSZ) powder anodes enabled by capillary suspension. The capillary suspension strategy can overcome the miscibility of liquid metal with other components, resulting in the self-standing and uniform LSZ powder anode. The nanothick eutectic gallium–indium (EGaIn) skin layer on Zn powders facilitated the horizontal growth of Zn along the (002) plane and mitigated Zn corrosion and hydrogen evolution reaction. Consequently, a full cell (V_2O_5 cathode || LSZ powder anode) exhibited a stable capacity retention per cycle of 99.99% over 2000 cycles at a fast current rate of 1 A g^{-1} , outperforming those of previously reported aqueous Zn full cells.



Despite their widespread application as a universal commodity power source in portable electronics, electric transportation, and grid-scale stationary energy storage,^{1,2} Li-ion batteries (LIBs) encounter challenges related to safety failures, high costs, and limited resources of core elements.^{3,4} As a potential solution, Zn-ion batteries (ZIBs) have garnered considerable attention owing to their high volumetric capacity (5855 mAh cm^{-3}), cost competitiveness, and the natural abundance of Zn. Moreover, their compatibility with aqueous electrolytes offers fast redox kinetics and safety tolerance.^{5–7}

Recently, Zn powder-based anodes have emerged as a promising alternative to conventional Zn foil-based counterparts, offering advantages such as low cost, tunable structures, and manufacturing scalability.⁸ However, the higher surface area of Zn powders compared to Zn foils exacerbates unwanted side reactions, including byproduct formation at Zn–electrolyte interfaces, Zn corrosion, and hydrogen evolution reaction (HER).⁹ Previous studies to overcome these challenges focused on incorporating conductive materials (e.g., MXene and graphene^{9,10}) and polymeric binders (e.g., polyacrylamide, polyethylene glycol, and oligomers^{11–13}). However, the electrical contacts between Zn powders and conductive materials are unstable during repeated Zn deposition/stripping cycles, and excessive polymeric binders reduce the electronic conductivity of the resulting anodes. In addition, the structural inhomogeneity of the anodes

accelerates side reactions, resulting in rapid cycle decay.¹⁴ Therefore, a new strategy for advanced Zn powder anodes, with an emphasis on the material chemistry and microstructure design, is required.

Here, we present a class of liquid metal-skinned Zn (LSZ) powder anodes using capillary suspension technology. Liquid metals, known for their structural deformability, high electronic conductivity, diverse processability, and self-healing properties, have a wide range of applications, including sensors, electronic circuits, and energy storage systems.^{15–18} However, their intrinsically high surface tension hinders their uniform dispersion with other components.¹⁹ In this study, we exploited the concept of a capillary suspension as a structural strategy to resolve this problem. Capillary suspension technology, driven by its ability to modulate rheological properties, has previously been reported in various fields, including 3D printing inks, porous films, and crack-free films.^{20–23} However, most of these approaches have predominantly explored the application of capillary forces in single-component particle suspensions. In contrast, we demonstrated

Received: April 11, 2024

Revised: May 10, 2024

Accepted: May 16, 2024

Published: May 20, 2024



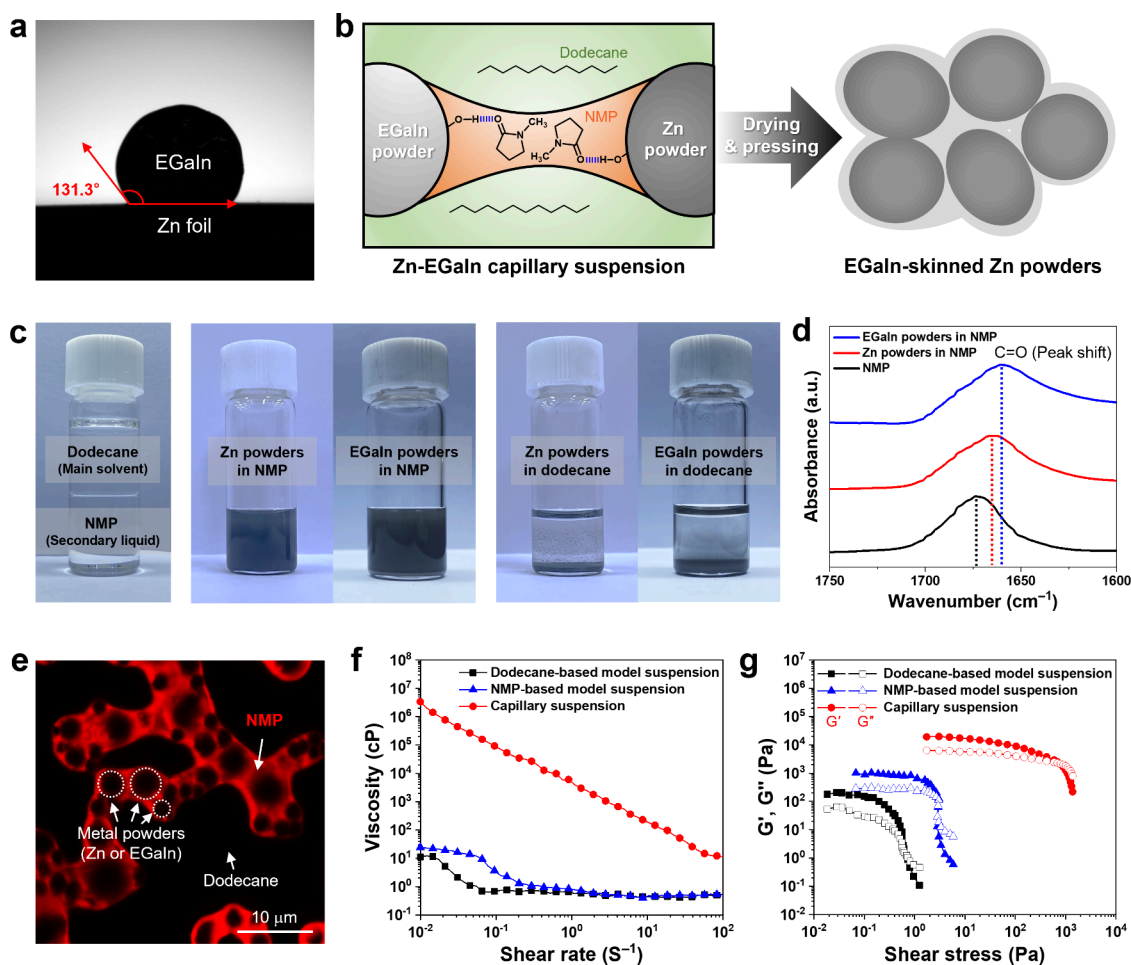


Figure 1. Design of the Zn-EGaIn capillary suspension. (a) Contact angle of the EGaIn on Zn foil. (b) Schematic illustration depicting the fabrication of the Zn-EGaIn capillary suspension and the resulting EGaIn-skinned Zn (LSZ) powders. (c) Photographs showing the solvent miscibility between NMP and dodecane (left), the dispersion state of Zn and EGaIn powders in NMP (middle), and dodecane (right) at room temperature. (d) Fourier transform infrared (FTIR) spectra of the NMP solvent, Zn powders in NMP, and EGaIn powders in NMP. (e) A confocal image of the capillary suspension measured with a 561 nm laser, in which a fluorescent dye (nile red) was added into NMP. (f) Viscosity of the capillary suspension and single-solvent-based model suspensions as a function of the shear rate. (g) Storage modulus (G') and loss modulus (G'') of the capillary suspension and single-solvent-based model suspensions as a function of shear stress.

the capillary suspension containing Zn and liquid metal (eutectic gallium–indium (EGaIn)) powders. Notably, to address the inherent challenges associated with the high surface tension of the liquid metals described above, we rationally designed the capillary suspension by formulating a solvent mixture consisting of a main solvent and a secondary immiscible liquid. Interconnected networks of Zn powders were uniformly formed in the capillary suspension while linked to the EGaIn powders via capillary bridges of the secondary liquid. After solvent drying and subsequent pressing, a self-standing LSZ powder anode was obtained, in which Zn powders were conformally coated with nanoscale EGaIn skin layers. The EGaIn skin layers acted as an electrically conductive glue, enabling the formation of polymeric binder-/carbon conductive additive-free LSZ powder anodes. The EGaIn skin layers allowed the horizontal growth of Zn along the (002) plane during Zn deposition-stripping cycles, preventing dendrite formation. Moreover, the EGaIn-mediated conformal coverage limited direct contact between the Zn powders and aqueous electrolytes, suppressing interfacial side reactions, such as Zn corrosion and HER, compared with a Zn foil anode with a lower surface area. Owing to these

advantages, the LSZ powder anode exhibited reliable cyclability for 2000 h in a symmetric cell. Additionally, a full cell (V_2O_5 cathode || LSZ powder anode) provided a stable capacity retention of 79.1% after 2000 cycles at a high current density of 1 A g^{-1} . Particularly, even at a faster current density of 10 A g^{-1} , the cell achieved a high capacity retention per cycle of 99.998% over 1000 cycles, outperforming those of previously reported aqueous Zn full cells. These results highlight the electrochemical viability of the liquid-metal-based capillary suspension approach in enabling the fabrication of practical Zn powder anodes with cycle sustainability and enhanced redox kinetics.

Owing to its high surface tension,²⁴ the EGaIn exhibited limited affinity with other metals (Figure 1a and Figure S1). To address this issue, we exploited a capillary suspension consisting of Zn powders linked to EGaIn powders via a capillary bridge formed by a secondary liquid (Figure 1b) to obtain EGaIn-skinned Zn (LSZ) powders.

To achieve structural stability in the capillary suspension, a solvent mixture composed of a main solvent and a secondary liquid was rationally designed based on the following criteria: 1) immiscibility of the two solvents, 2) distinct compatibility

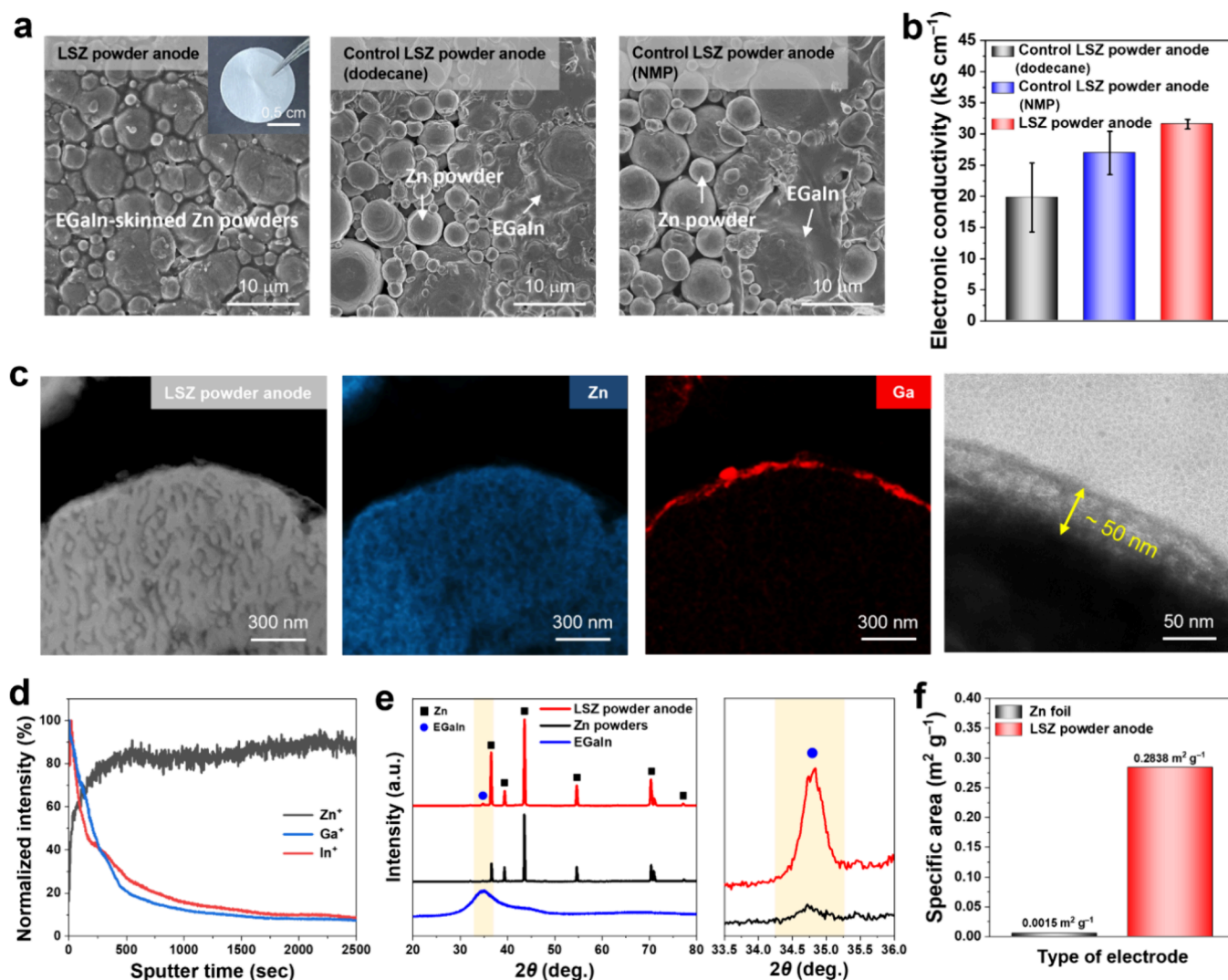


Figure 2. Fabrication of the LSZ powder anodes and their physicochemical characteristics. (a) Surface field emission scanning electron microscopy (FE-SEM) images of the LSZ powder anodes fabricated using capillary suspension (left; an inset is a photograph of the LSZ powder anode), dodecane-based (middle), and NMP-based (right) model suspensions. (b) Electronic conductivity of the LSZ powder anode and control LSZ powder anodes (fabricated using the dodecane or NMP-based model suspensions). (c) Transmission electron microscopy (TEM) and corresponding energy dispersive spectroscopy (EDS) mapping images (focusing on Zn and Ga elements) of the LSZ powder. (d) Time-of-flight secondary-ion mass spectrometry (TOF-SIMS) depth profiles of the LSZ powder anode. (e) X-ray diffraction (XRD) patterns of the EGaIn, Zn powders, and LSZ powder anode. (f) Specific surface area of the Zn foil and LSZ powder anodes.

with Zn and EGaIn powders, and 3) chemical stability with the metal powders. Accordingly, dodecane and *N*-methyl-2-pyrrolidone (NMP) were selected as the main solvent and secondary liquid, respectively (Figure S2 and Table S1). These two solvents were immiscible owing to their disparate polar indices (0.1 for dodecane vs 6.7 for NMP; Figure 1c, left). The morphologies of Zn and EGaIn powders are shown in Figure S3. Notably, NMP facilitated the dispersion of Zn and EGaIn powders (Figure 1c, middle), whereas sedimentation occurred in dodecane due to poor compatibility with metal powders (Figure 1c, right). This finding was corroborated by Fourier-transform infrared (FTIR) spectroscopy analysis of the model suspensions (Zn or EGaIn powders dispersed in a single solvent of dodecane or NMP). A downshift in the characteristic carbonyl peak (C=O) assigned to NMP at 1675 cm⁻¹ was observed in the FTIR spectrum of the NMP-based model suspension (Figure 1d and Figure S4), indicating dipole-dipole interaction^{25,26} between the carbonyl group of NMP

and hydroxyl group (–OH) of the metal powders. In contrast, no shift was observed in the FTIR peaks of the dodecane-based model suspension (Figure S5).

Based on this understanding, a Zn-EGaIn capillary suspension was prepared using a solvent mixture of dodecane/NMP = 90/10 (v/v). The microstructure of the resulting Zn-EGaIn capillary suspension was observed through confocal microscopy analysis (Figure 1e), where NMP was stained with a fluorescent dye (nile red) to confirm the presence of capillary bridges. The interconnected metal powders (EGaIn and Zn) were observed to be uniformly linked by the capillary bridges of NMP. Additionally, the formation of powder networks was further confirmed by examining the rheological properties of the capillary suspensions (Figure 1f). The capillary suspension, influenced by capillary force (F_c),^{27,28} exhibited a higher viscosity compared to the model suspensions (containing a single solvent of dodecane or NMP). In addition, the optimal ratio of

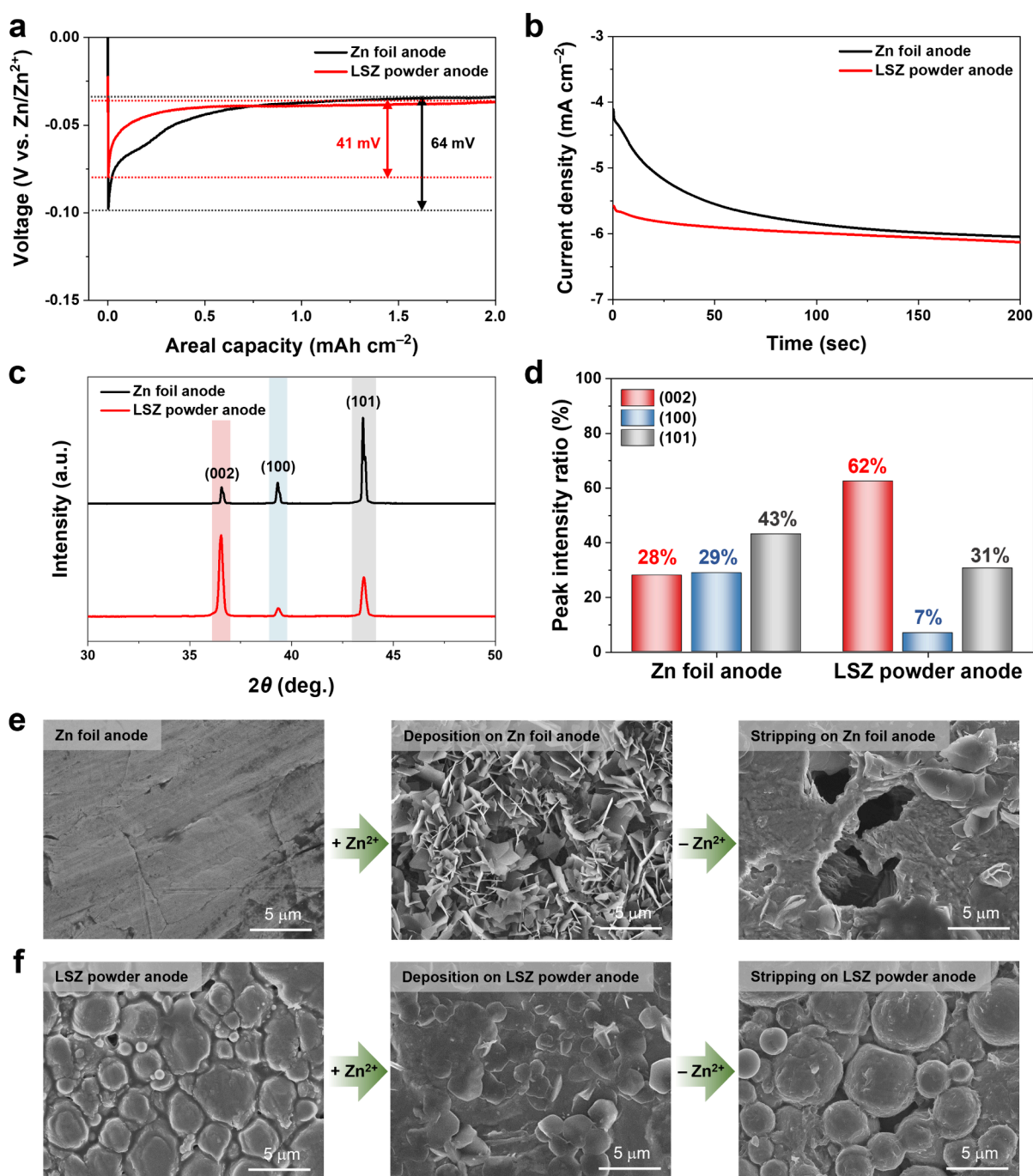


Figure 3. Zn deposition/stripping behavior of the LSZ powder anodes. (a) Voltage profiles of the Zn deposition on the LSZ powder and Zn foil anodes at a current density of 0.2 mA cm^{-2} . (b) Chronoamperometry (CA) curves of the LSZ powder and Zn foil anodes at -150 mV . (c) XRD pattern and (d) peak intensity ratios of (002), (100), and (101) planes in the LSZ powder and Zn foil anodes after Zn deposition at a current density of 0.2 mA cm^{-2} and an areal capacity of 2 mAh cm^{-2} . Surface FE-SEM images of (e) Zn foil and (f) LSZ powder anodes after the Zn deposition/stripping cycle at a current density of 0.2 mA cm^{-2} and an areal capacity of 2 mAh cm^{-2} .

dodecane/NMP to form a stable capillary suspension was determined by rheological evaluations (Figure S6). The highest viscosity was observed at a dodecane/NMP ratio of 90/10, indicating that this ratio was effective in forming the capillary suspension. Based on this result, the ratio of dodecane/NMP = 90/10 (v/v) was determined as the optimal point for establishing a stable capillary suspension. Meanwhile, the capillary suspension and model suspensions showed that the storage modulus (G') was higher than the loss modulus (G'') in the low shear stress region, and the opposite trend was

observed in the high shear stress region, indicating a typical viscoelastic fluid behavior^{29,30} (Figure 1g). The yield stress (τ_y), determined by the intersection of G' and G'' , of the capillary suspension (823.83 Pa) was much higher than those of the NMP-based (2.95 Pa) and dodecane-based (0.62 Pa) model suspensions. These results demonstrated the presence of well-established interconnected networks in the capillary suspension, which is mainly attributed to the formation of capillary bridges between the powders. Furthermore, compared to the immediate precipitation observed in the model

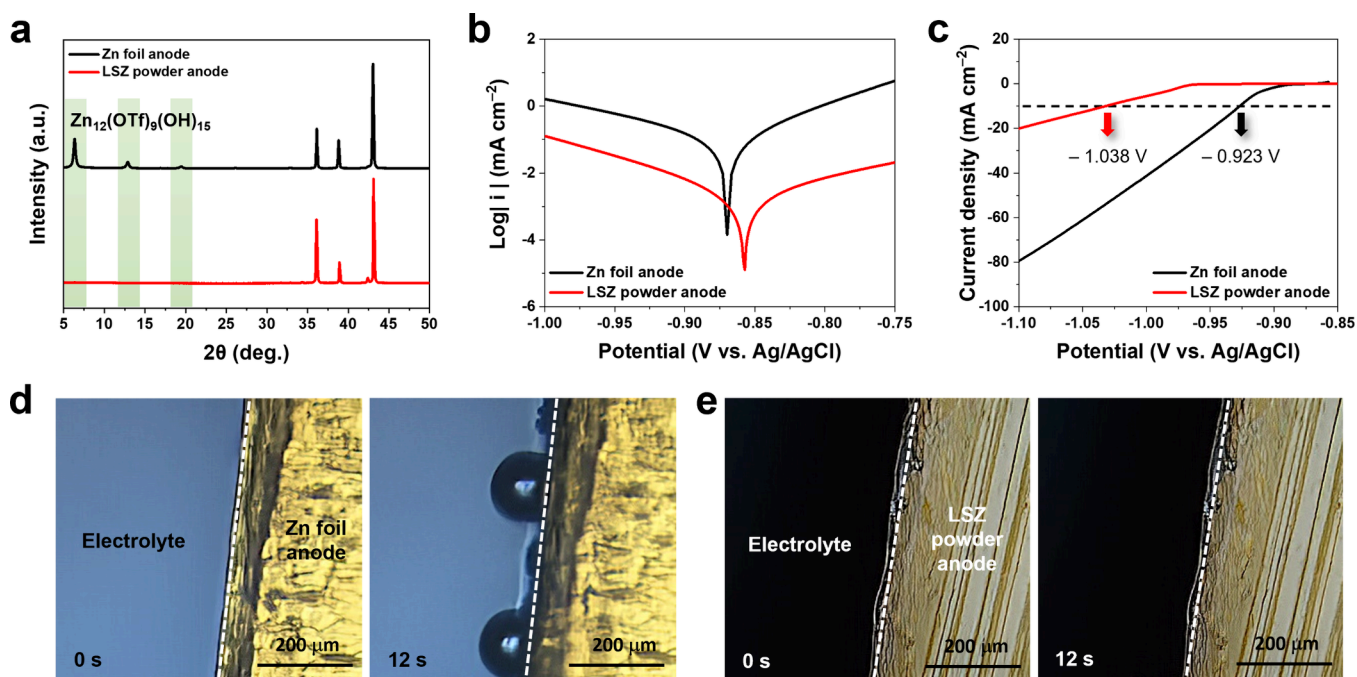


Figure 4. Zn corrosion and hydrogen evolution reaction (HER) of the LSZ powder anodes. (a) XRD patterns of the LSZ powder and Zn foil anodes after immersion in an aqueous electrolyte (4 m Zn(OTf)₂) for 48 h. (b) Tafel plots and (c) linear sweep voltammetry (LSV) curves of the LSZ powder and Zn foil anodes, in which the LSZ powder and Zn foil were used as the working electrodes, the Zn plate as the counter electrode, and Ag/AgCl as the reference electrode. *In situ* optical microscopy (OM) images of (d) Zn foil anode and (e) LSZ powder anode in transparent cell (LSZ powder (or Zn foil) during the CA tests at -1 V (vs Zn/Zn²⁺).

suspensions, the capillary suspension maintained a dispersed state for 7 days (Figures S7 and S8). These results affirm the formation of interconnected networks of metal powders in the Zn-EGaIn capillary suspension.

The as-prepared capillary suspension was dried to eliminate the solvent mixture and then pressed to obtain the self-standing LSZ powder anodes. Meanwhile, control LSZ powder anodes were fabricated by using the model suspensions containing a single solvent. The LSZ powder anode displayed a uniform dispersion of Zn and EGaIn powders, which was attributed to the well-interconnected powder networks formed in the capillary suspension (Figure 2a, left and Figure S9). In contrast, the control LSZ powder anodes exhibited randomly and unevenly dispersed Zn and EGaIn powders, indicating the poor structural stability in the model suspensions and nonuniform powder migration during solvent evaporation.^{31,32} This disparity in the dispersion states was verified through electronic conductivity measurements (Figure 2b). The LSZ powder anode exhibited a higher electronic conductivity than the control LSZ powder anodes, signifying the formation of highly percolated electronic networks. These findings underscore the effectiveness of capillary suspensions in addressing the inherent dispersion challenges associated with liquid metals.

Transmission electron microscopy (TEM) and corresponding energy dispersive spectroscopy (EDS) images of the LSZ powder anode revealed a uniform nanothick (~ 50 nm) EGaIn layer covering the Zn powders (Figure 2c). This unique structure was further elucidated through time-of-flight secondary-ion mass spectrometry (TOF-SIMS) depth profiles (Figure 2d), which indicated the predominant presence of Ga and In near the surface, consistent with TEM results. X-ray diffraction (XRD) patterns confirmed the existence of the EGaIn skin layer and the preservation of the crystalline

structure of Zn in the LSZ powder anode (Figure 2e). The mass ratio of elements (Ga and In) in the LSZ powder was determined to be 6.2 wt % through inductively coupled plasma optical emission spectrometry (ICP-OES) analysis (Figure S10).

The specific surface area of the LSZ powder anode was estimated by using Brunauer–Emmett–Teller (BET) analysis (Figure 2f). The LSZ powder anode exhibited a significantly higher surface area compared to Zn foil, indicating that the thin and conformal coverage of Zn powders by the EGaIn skin layer did not compromise the porous structure of the LSZ powder anode. Moreover, the thicknesses of the LSZ powder anodes ranged from 30 to 169 μm (Figure S11), demonstrating the tunability of their areal capacities and the feasibility of designing full cells with various electrochemical metrics.

The Zn nucleation overpotential of the LSZ powder anode was investigated at a current density of 0.2 mA cm⁻² (Figure 3a). The LSZ powder anode exhibited a lower nucleation overpotential (41 mV) compared to that of the Zn foil anode (64 mV). This enhancement can be attributed to the higher surface area of the LSZ powder anode, leading to a reduction in local current density.³³ Additionally, chronoamperometry (CA) analysis of the anodes was performed to monitor the change in current density over time (Figure 3b). A continuous increase in current density indicates promoted Zn dendrite growth.^{34,35} In this study, the current density of the Zn foil anode increased continuously over 100 s, whereas the current density of the LSZ powder anode reached an equilibrium state within a shorter time, indicating suppression of Zn dendrite growth.

The peak intensity ratios of (002), (100), and (101)³⁶ planes in the XRD patterns of the anodes after Zn deposition were analyzed (Figure 3c and d). The LSZ powder anode exhibited preferential growth of Zn along the (002) plane

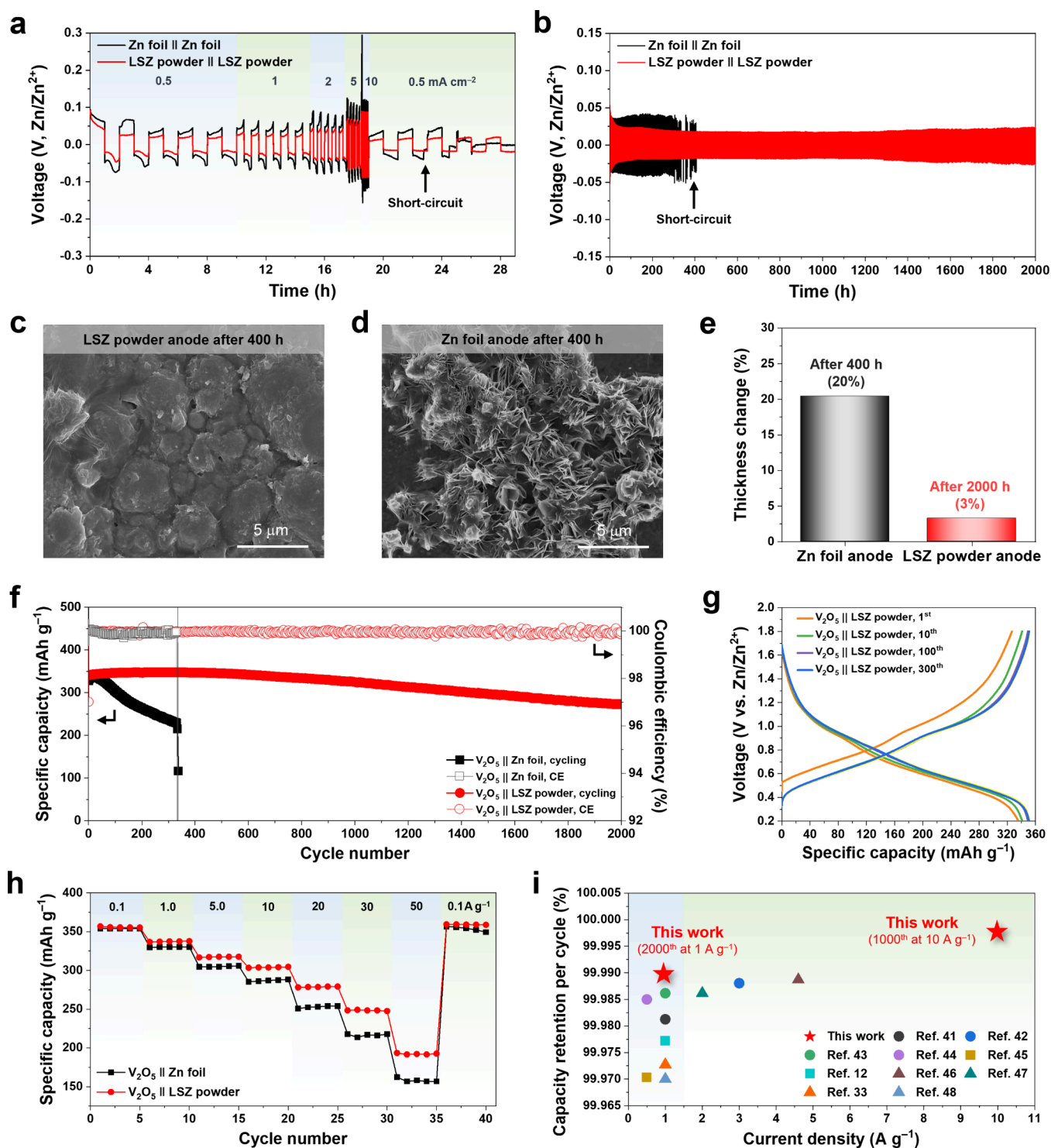


Figure 5. Electrochemical performance of the LSZ powder anodes. (a) Rate capability of the symmetrical cells (LSZ powder || LSZ powder and Zn foil || Zn foil) at various current densities from 0.5 to 10 mA cm⁻² and an areal capacity of 0.5 mAh cm⁻². (b) Voltage profiles of the symmetric cells at a current density of 1 mA cm⁻² and an areal capacity of 0.5 mAh cm⁻². Surface FE-SEM images of (c) LSZ powder and (d) Zn foil anodes after the cycling test (400 h) of the symmetric cells. (e) Change in the thickness of the symmetric cells after the cycling test. (f) Cycling performance of the full cells (V₂O₅ cathode || LSZ powder (or Zn foil) anode) and (g) voltage profiles (1st, 10th, 100th, and 300th cycles) of the full cell (V₂O₅ cathode || LSZ powder anode) at a current density of 1 A g⁻¹. (h) Rate capability of the full cells at various current densities from 0.1 to 50 A g⁻¹. (i) Comparison of the capacity retention per cycle of the full cell assembled with the LSZ powder anode (this work) and previously reported aqueous Zn full cells as a function of the current density.

compared with the (100) and (101) planes, suggesting horizontal Zn growth in the LSZ powder anode. This result aligns with the findings of a previous study,³⁷ which reported the conformal Zn deposition on the epitaxial interface (In

GaZn₆O₉) formed via spontaneous alloying between EGaIn and Zn. It is noted that the highly oriented Zn (002) plane shows planar surfaces with restricted dendrite growth and lower chemical activity, thereby mitigating interfacial side

reactions.^{38,39} In contrast, higher peak intensities of the (100) and (101) planes were observed in the Zn foil anode.

These results were further corroborated by comparing the morphologies of the LSZ powder and Zn foil anodes after the Zn deposition/stripping cycle (Figure 3e and f). The cycled Zn foil anode showed random and nonuniform Zn dendrite growth after Zn deposition and a severely disrupted structure after subsequent Zn stripping. In contrast, the LSZ powder anode exhibited homogeneous and dense Zn deposition without noticeable dendrite growth and returned to its initial state after Zn stripping, demonstrating superior electrochemical reliability during the cycling test.

Zn powder anodes are known to experience severe interfacial side reactions with aqueous electrolytes owing to their extensive surface area.^{9,11} In this study, the corrosion reactions of LSZ powder and Zn foil anodes were investigated after immersion in an aqueous electrolyte (4 m zinc trifluoromethanesulfonate ($Zn(OTf)_2$) for 48 h (Figure 4a). The Zn foil anode exhibited distinct peaks at 6.4, 12.9, and 19.5°, corresponding to $Zn_{12}(OTf)_9(OH)_{15}\cdot nH_2O$ (JCPDS card no. 41–1421), a common byproduct⁴⁰ formed when Zn metals are exposed to aqueous electrolytes. In contrast, the LSZ powder anode did not show these byproduct peaks, indicating the viability of the EGaIn skin layer on Zn powders in preventing corrosion reactions. The corrosion stability of the LSZ powder anode was further confirmed through Tafel plot analysis (Figure 4b). The LSZ powder anode exhibited a higher corrosion potential (-0.858 V vs Ag/AgCl) and a lower corrosion current (0.013 mA cm^{-2}) compared to the Zn foil anode.

The HER of LSZ powder and Zn foil anodes was investigated by using linear sweep voltammetry (LSV; Figure 4c). The onset potential for hydrogen evolution of the LSZ powder anode (-1.038 V at -20 mA cm^{-2}) was significantly lower than that of the Zn foil anode (-0.923 V), demonstrating the effective suppression of HER. The occurrence of HER at the electrolyte–anode interface was visualized using *in situ* optical microscopy (OM) analysis in transparent cells (LSZ powder (or Zn foil) || Zn foil) during chronoamperometry (CA) at -1 V (vs Zn/Zn^{2+}) (Figure 4d and e). The Zn foil anode exhibited rapid hydrogen gas generation within 12 s, whereas a detectable level of HER was not observed in the LSZ powder anode (Movies S1 and S2).

Next, we compared the rate capabilities of LSZ powder and Zn foil anodes using symmetric cells (LSZ powder || LSZ powder and Zn foil || Zn foil) at various current densities ranging from 0.5 to 10 mA cm^{-2} and an areal capacity of 0.5 mAh cm^{-2} (Figure 5a). The LSZ powder anode showed stable Zn deposition/stripping behavior along with lower polarization voltage over the entire range of current densities compared with the Zn foil anode. This improvement was attributed to the effective suppression of the Zn dendrite growth and interfacial side reactions. Electrochemical reversibility of the Zn deposition/stripping cycle was assessed at a current density of 1 mA cm^{-2} and an areal capacity of 0.5 mAh cm^{-2} (Figure 5b). The LSZ powder anode demonstrated a superior cycling performance over 2000 h, whereas the Zn foil anode experienced a short circuit after approximately 400 h. This advantageous effect of the LSZ powder anode was further underscored by making a comparison with those of the previous works at the same current density of 1 mA cm^{-2} (Table S2). The LSZ powder showed improved cycle stability compared to previous works, demonstrating the effectiveness

of the LSZ powder anode. Furthermore, the LSZ powder anode exhibited stable cycle retention over 450 h, even at a higher current density of 5 mA cm^{-2} (Figure S12).

The structural changes in the cycled anodes (after 400 h, Figure 5b) were investigated (Figure 5c and d). The LSZ powder anode maintained a smooth and uniform surface with negligible formation of Zn dendrites, whereas the Zn foil anode displayed a sharp and random growth of Zn dendrites. Electrochemical impedance spectroscopy (EIS) analysis of the symmetric cells indicated a smaller increase in the charge-transfer resistance (R_{ct}) of the LSZ powder anode ($26 \rightarrow 142$ Ω) after the cycling test (400 h) compared to the Zn foil anode cell ($58 \rightarrow 878$ Ω) (Figure S13), signifying suppressed undesired interfacial side reactions with the aqueous electrolyte. Measurements of the change in thickness of the symmetric cells after the cycling test (Figure 5e) revealed a substantial increase in thickness for the Zn foil anode, indicating vigorous HER. In contrast, the LSZ powder symmetric cell exhibited a minimal increase in thickness ($\sim 3\%$) even after 2000 h, demonstrating effective suppression of HER at the LSZ powder anode.

To underscore the advantageous effect of the LSZ powder anode, a Zn powder anode was prepared as a control sample by mixing pristine Zn powders, carbon black conductive additive, and poly(vinylidene fluoride) (PVdF) binder, in which the composition ratio of Zn powder/carbon black/PVdF binder was 94/3/3 (w/w/w). The morphology and electronic conductivity of the fabricated Zn powder anode are shown in Figures S14 and S15, respectively. The symmetric cell with the Zn powder anode showed unstable Zn deposition/stripping cycle behavior and was eventually short-circuited along with cell explosion after 330 h (Figures S16 and S17). This failure was attributed to the high surface area of Zn powders, which accelerated the HER. Additionally, a dendritic and irregular Zn morphology was observed in the Zn powder anode after the cycling test (Figure S18). These results highlight that the improved cyclability of the LSZ powder anode can be attributed to the conformal coverage of Zn powders by the EGaIn skin layer.

The LSZ powder anode was paired with a V_2O_5 cathode (areal mass loading = 1.3 mg cm^{-2}) to fabricate a Zn full cell. The full cell with the LSZ powder anode exhibited higher capacity retention (= 79.1% after 2000 cycles) at a current density of 1 A g^{-1} compared to the control full cell with the Zn foil anode, which lost its electrochemical activity after 337 cycles (Figures 5f,g and S19). Furthermore, the full cell with the LSZ powder anode exhibited better rate performance at various current densities from 0.1 to 50 A g^{-1} (Figure 5h). Additionally, the full cell with the LSZ powder anode demonstrated superior cyclability, even at a higher current density of 10 A g^{-1} (Figure S20). As another control sample, we fabricated a full cell composed of a Zn powder anode and V_2O_5 cathode. The full cell with the Zn powder anode showed significantly lower capacity retention (= 27.6% after 300 cycles) compared to the LSZ powder anode at a current density of 1 A g^{-1} (Figure S21).

This enhanced cycling performance of the full cell assembled with the LSZ powder anode was further emphasized by making a comparison with those of previously reported Zn full cells^{12,33,41–48} (Figure 5i and Table S3). The full cell with the LSZ powder anode exhibited a higher capacity retention per cycle of 99.990% for 2000 cycles at 1 A g^{-1} and 99.998% for 1000 cycles even at 10 A g^{-1} , outperforming those of

previously reported aqueous Zn full cells. These results demonstrate the potential utilization of the LSZ powder anode for practical Zn full cells with reliable cycle life even under fast current rates. In addition, the cycling stability of this study could be further improved by the use of advanced electrolytes.^{49–51}

In summary, we presented a polymeric binder-/carbon conductive additive-free, self-standing LSZ (EGaIn-skinned Zn) powder anode enabled by a capillary suspension. The rationally designed solvent mixture (comprising dodecane as the main solvent and NMP as the secondary immiscible liquid) in the capillary suspension allowed for the formation of interconnected networks of Zn powders linked to the EGaIn powders via capillary bridges. The EGaIn skin layer on the Zn powders facilitated horizontal Zn growth along the (002) plane, contributing to dendrite-free Zn deposition. Furthermore, the EGaIn skin layer restricted direct contact of Zn powders with the aqueous electrolyte, effectively suppressing Zn corrosion and the HER despite the high surface area of the LSZ powder anode. Driven by these advantageous effects, the LSZ powder anode exhibited a stable cyclability for 2000 h in a symmetric cell. Additionally, the full cell (V₂O₅ cathode || LSZ powder anode) exhibited superior capacity retention (= 79.1% after 2000 cycles) at 1 A g⁻¹ and a capacity retention per cycle of 99.998% over 1000 cycles at 10 A g⁻¹, surpassing those of previously reported aqueous Zn full cells. The LSZ powder anode, developed through the capillary suspension, can be suggested as a promising alternative to conventional Zn foil anodes and holds potential as a versatile platform technology applicable to emerging metal battery systems in the pursuit of powder-based anodes.

■ ASSOCIATED CONTENT

SI Supporting Information

The Supporting Information is available free of charge at <https://pubs.acs.org/doi/10.1021/acseenergylett.4c01009>.

Hydrogen gas evolution of Zn foil movie (MP4)

Hydrogen gas evolution of LSZ powder movie (MP4)

Experimental methods (materials, preparation of electrodes, characterizations, and electrochemical analysis), supporting figures (contact angle, FE-SEM images, EDS mappings, FTIR spectra, photographs, ICP-OES results, EIS curves, thickness change results, voltage profiles, and cycling performance), and supporting tables (specification of solvents and comparison of the electrochemical performance) (DOCX)

■ AUTHOR INFORMATION

Corresponding Authors

Zhong-Shuai Wu – State Key Laboratory of Catalysis, Dalian Institute of Chemical Physics, Chinese Academy of Sciences, Dalian 116023, China; orcid.org/0000-0003-1851-4803; Email: wuzs@dicp.ac.cn

Sang-Young Lee – Department of Chemical and Biomolecular Engineering, Yonsei University, Seoul 03722, Republic of Korea; orcid.org/0000-0001-7153-0517; Email: syleek@yonsei.ac.kr

Authors

Hyunseo Kang – Department of Chemical and Biomolecular Engineering, Yonsei University, Seoul 03722, Republic of Korea; orcid.org/0009-0009-3392-8685

Seung-Hyeok Kim – Department of Chemical and Biomolecular Engineering, Yonsei University, Seoul 03722, Republic of Korea; Pritzker School of Molecular Engineering, The University of Chicago, Chicago, Illinois 60637, United States

David B. Ahn – Department of Chemistry, Ulsan National Institute of Science and Technology (UNIST), Ulsan 44919, Republic of Korea

Xiao Wang – State Key Laboratory of Catalysis, Dalian Institute of Chemical Physics, Chinese Academy of Sciences, Dalian 116023, China

Complete contact information is available at:

<https://pubs.acs.org/10.1021/acseenergylett.4c01009>

Author Contributions

^{||}H.K. and S.-H.K. authors contributed equally to this paper. H.K., S.-H.K., and D.B.A. designed all electrochemical experiments and analyzed the results. X.W. synthesized the vanadium oxide. H.K. and S.-H.K. prepared the manuscript. Z.-S.W. and S.-Y.L. revised the manuscript critically. All authors have given approval for the final version of the manuscript.

Notes

The authors declare no competing financial interest.

■ ACKNOWLEDGMENTS

This work was supported by National Research Foundation of Korea (NRF) grants funded by the Korean Government (MSIP) (RS-2024-00344021 and RS-2023-00261543).

■ REFERENCES

- (1) Chen, Y.; Zhao, B.; Yang, Y.; Cao, A. Toward High-Areal-Capacity Electrodes for Lithium and Sodium Ion Batteries. *Adv. Energy Mater.* **2022**, *12* (44), 2201834.
- (2) Duffner, F.; Kronmeyer, N.; Tübke, J.; Leker, J.; Winter, M.; Schmich, R. Post-Lithium-Ion Battery Cell Production and Its Compatibility with Lithium-Ion Cell Production Infrastructure. *Nat. Energy* **2021**, *6*, 123–134.
- (3) Yin, Y.; Yang, Y.; Cheng, D.; Mayer, M.; Holoubek, J.; Li, W.; Raghavendran, G.; Liu, A.; Lu, B.; Davies, D. M.; et al. Fire-Extinguishing, Recyclable Liquefied Gas Electrolytes for Temperature-Resilient Lithium-Metal Batteries. *Nat. Energy* **2022**, *7*, 548–559.
- (4) Feng, X.; Ren, D.; He, X.; Ouyang, M. Mitigating Thermal Runaway of Lithium-Ion Batteries. *Joule* **2020**, *4* (4), 743–770.
- (5) Wu, K.; Huang, J.; Yi, J.; Liu, X.; Liu, Y.; Wang, Y.; Zhang, J.; Xia, Y. Recent Advances in Polymer Electrolytes for Zinc Ion Batteries: Mechanisms, Properties, and Perspectives. *Adv. Energy Mater.* **2020**, *10* (12), 1903977.
- (6) Li, X.; Wang, L.; Fu, Y.; Dang, H.; Wang, D.; Ran, F. Optimization strategies toward advanced aqueous zinc-ion batteries: From facing key issues to viable solutions. *Nano Energy* **2023**, *116*, 108858.
- (7) Tang, B.; Shan, L.; Liang, S.; Zhou, J. Issues and Opportunities Facing Aqueous Zinc-Ion Batteries. *Energy Environ. Sci.* **2019**, *12* (11), 3288–3304.
- (8) Li, Q.; Wang, Y.; Mo, F.; Wang, D.; Liang, G.; Zhao, Y.; Yang, Q.; Huang, Z.; Zhi, C. Calendar Life of Zn Batteries Based on Zn Anode with Zn Powder/Current Collector Structure. *Adv. Energy Mater.* **2021**, *11* (14), 2003931.
- (9) Li, X.; Li, Q.; Hou, Y.; Yang, Q.; Chen, Z.; Huang, Z.; Liang, G.; Zhao, Y.; Ma, L.; Li, M.; et al. Toward a Practical Zn Powder Anode: Ti₃C₂T_x MXene as a Lattice-Match Electrons/Ions Redistributor. *ACS Nano* **2021**, *15* (9), 14631–14642.
- (10) Du, W.; Huang, S.; Zhang, Y.; Ye, M.; Li, C. C. Enable commercial Zinc powders for dendrite-free Zinc anode with improved

utilization rate by pristine graphene hybridization. *Energy Storage Mater.* **2022**, *45*, 465–473.

(11) Yang, Z.; Zhang, Q.; Li, W.; Xie, C.; Wu, T.; Hu, C.; Tang, Y.; Wang, H. A Semi-Solid Zinc Powder-Based Slurry Anode for Advanced Aqueous Zinc-Ion Batteries. *Angew. Chem., Int. Ed.* **2023**, *62* (3), No. e202215306.

(12) Huyan, X.; Yi, Z.; Sang, Z.; Tan, S.; Liu, J.; Chen, R.; Si, W.; Liang, J.; Hou, F. Polyethylene glycol coating on zinc powder surface: Applications in dendrite-free zinc anodes with enhanced utilization rate. *Appl. Surf. Sci.* **2023**, *614*, 156209.

(13) Cao, C.; Zhou, K.; Du, W.; Li, C. C.; Ye, M.; Zhang, Y.; Tang, Y.; Liu, X. Designing Soft Solid-like Viscoelastic Zinc Powder Anode toward High-Performance Aqueous Zinc-Ion Batteries. *Adv. Energy Mater.* **2023**, *13* (38), 2301835.

(14) Yang, J.; Xu, X.; Gao, Y.; Wang, Y.; Cao, Q.; Pu, J.; Bu, F.; Meng, T.; Guan, C. Ultra-Stable 3D-Printed Zn Powder-Based Anode Coated with a Conformal Ion-Conductive Layer. *Adv. Energy Mater.* **2023**, *13* (40), 2301997.

(15) Li, G.; Zhang, M.; Liu, S.; Yuan, M.; Wu, J.; Yu, M.; Yeng, L.; Xu, Z.; Guo, J.; Li, G.; et al. Three-Dimensional Flexible Electronics Using Solidified Liquid Metal with Regulated Plasticity. *Nat. Electron.* **2023**, *6*, 154–163.

(16) Heng, W.; Solomon, S.; Gao, W. Flexible Electronics and Devices as Human-Machine Interfaces for Medical Robotics. *Adv. Mater.* **2022**, *34* (16), 2107902.

(17) Guo, X.; Ding, Y.; Xue, L.; Zhang, L.; Zhang, C.; Goodenough, J. B.; Yu, G. A Self-Healing Room-Temperature Liquid-Metal Anode for Alkali-Ion Batteries. *Adv. Funct. Mater.* **2018**, *28* (46), 1804649.

(18) Liu, C.; Luo, Z.; Deng, W.; Wei, W.; Chen, L.; Pan, A.; Ma, J.; Wang, C.; Zhu, L.; Xie, L.; et al. Liquid Alloy Interlayer for Aqueous Zinc-Ion Battery. *ACS Energy Lett.* **2021**, *6* (2), 675–683.

(19) Chang, H.; Guo, R.; Sun, Z.; Wang, H.; Hou, Y.; Wang, Q.; Rao, W.; Liu, J. Direct Writing and Repairable Paper Flexible Electronics Using Nickel-Liquid Metal Ink. *Adv. Mater. Interfaces* **2018**, *5* (20), 1800571.

(20) Dunstan, T. S.; Das, A. A. K.; Starck, P.; Stoyanov, S. D.; Paunov, V. N. Capillary structured suspensions from in situ hydrophobized calcium carbonate particles suspended in a polar liquid media. *Langmuir* **2018**, *34* (1), 442–452.

(21) Ding, H.; Barg, S.; Derby, B. Direct 3D printing of graphene using capillary suspensions. *Nanoscale* **2020**, *12*, 11440–11447.

(22) Maurath, J.; Dittmann, J.; Schultz, N.; Willenbacher, N. Fabrication of highly porous glass filters using capillary suspension processing. *Sep. Purif. Technol.* **2015**, *149*, 470–478.

(23) Schneider, M.; Maurath, J.; Fischer, S. B.; Weiß, M.; Willenbacher, N.; Koos, E. Suppressing Crack Formation in Particulate Systems by Utilizing Capillary Forces. *ACS Appl. Mater. Interfaces* **2017**, *9*, 11095–11105.

(24) Park, Y.-G.; Min, H.; Kim, H.; Zhexembekova, A.; Lee, C. Y.; Park, J.-U. Three-Dimensional, High-Resolution Printing of Carbon Nanotube/Liquid Metal Composites with Mechanical and Electrical Reinforcement. *Nano Lett.* **2019**, *19* (8), 4866–4872.

(25) Yau, H. C.; Bayazit, M. K.; Steinke, J. H.; Shaffer, M. S. Sonochemical Degradation of N-Methylpyrrolidone and Its Influence on Single Walled Carbon Nanotube Dispersion. *Chem. Commun.* **2015**, *51* (93), 16621–16624.

(26) Li, Q.; Sun, X.; Lozano, K.; Mao, Y. Asymmetric supercapacitors with dominant pseudocapacitance based on manganese oxide nanoflowers in a neutral aqueous electrolyte. *RSC Adv.* **2013**, *3* (47), 24886–24890.

(27) Georgiev, M. T.; Danov, K. D.; Kralchevsky, P. A.; Gurkov, T. D.; Krusteva, D. P.; Arnaudov, L. N.; Stoyanov, S. D.; Pelan, E. G. Rheology of particle/water/oil three-phase dispersions: Electrostatics vs. capillary bridge forces. *J. Colloid Interface Sci.* **2018**, *513*, 515–526.

(28) Bossler, F.; Koos, E. Structure of particle networks in capillary suspensions with wetting and nonwetting fluids. *Langmuir* **2016**, *32* (6), 1489–1501.

(29) Kim, S.-H.; Choi, K.-H.; Cho, S.-J.; Choi, S.; Park, S.; Lee, S.-Y. Printable solid-state lithium-ion batteries: A new route toward shape-

conformable power sources with aesthetic versatility for flexible electronics. *Nano Lett.* **2015**, *15* (8), 5168–5177.

(30) Lee, S.-S.; Kim, S.-H.; Ahn, D. B.; Lee, K.-H.; Jo, Y.; Jeong, S.; Lee, S.-Y. All-Direct-Ink-Writing of Artistic Supercapacitors: Toward On-Demand Embodied Power Sources. *Adv. Funct. Mater.* **2022**, *32* (34), 2202901.

(31) Zhang, Y. S.; Courtier, N. E.; Zhang, Z.; Liu, K.; Bailey, J. J.; Boyce, A. M.; Richardson, G.; Shearing, P. R.; Kendrick, E.; Brett, D. J. L. A Review of Lithium-Ion Battery Electrode Drying: Mechanisms and Metrology. *Adv. Energy Mater.* **2022**, *12* (2), 2102233.

(32) Park, J.; Ahn, K. H. Controlling Drying Stress and Mechanical Properties of Battery Electrodes Using a Capillary Force-Induced Suspension System. *Ind. Eng. Chem. Res.* **2021**, *60* (13), 4873–4882.

(33) Yu, H.; Zeng, Y.; Li, N. W.; Luan, D.; Yu, L.; Lou, X. W. Confining Sn Nanoparticles in Interconnected N-Doped Hollow Carbon Spheres as Hierarchical Zincophilic Fibers for Dendrite-Free Zn Metal Anode. *Sci. Adv.* **2022**, *8* (10), No. eabm5766.

(34) Xie, S.; Li, Y.; Li, X.; Zhou, Y.; Dang, Z.; Rong, J.; Dong, L. Stable Zinc Anodes Enabled by Zincophilic Cu Nanowire Networks. *Nano-Micro Lett.* **2022**, *14* (1), 39.

(35) Xi, M.; Liu, Z.; Ding, J.; Cheng, W.; Jia, D.; Lin, H. Saccharin Anion Acts as a “Traffic Assistant” of Zn²⁺ to Achieve a Long-Life and Dendritic-Free Zinc Plate Anode. *ACS Appl. Mater. Interfaces* **2021**, *13* (25), 29631–29640.

(36) Zheng, J.; Zhao, Q.; Tang, T.; Yin, J.; Quilty, C. D.; Renderos, G. D.; Liu, X.; Deng, Y.; Wang, L.; Bock, D. C.; et al. Reversible Epitaxial Electrodeposition of Metals in Battery Anodes. *Science* **2019**, *366* (6465), 645–648.

(37) Zou, J.; Zeng, Z.; Wang, C.; Zhu, X.; Zhang, J.; Lan, H.; Li, L.; Yu, Y.; Wang, H.; Zhu, X.; et al. Ultraconformal Horizontal Zinc Deposition Toward Dendrite-Free Anode. *Small Struct.* **2023**, *4* (1), 2200194.

(38) Yuan, W. T.; Nie, X. Y.; Ma, G. Q.; Liu, M. Y.; Wang, Y. Y.; Shen, S. G.; Zhang, N. Realizing Textured Zinc Metal Anodes through Regulating Electrodeposition Current for Aqueous Zinc Batteries. *Angew. Chem., Int. Ed.* **2023**, *62* (10), No. e202218386.

(39) Zheng, Z.; Zhong, X.; Zhang, Q.; Zhang, M.; Dai, L.; Xiao, X.; Xu, J.; Jiao, M.; Wang, B.; Li, H.; et al. An extended substrate screening strategy enabling a low lattice mismatch for highly reversible zinc anodes. *Nat. Commun.* **2024**, *15*, 753.

(40) Liu, X.; Euchner, H.; Zarrabeitia, M.; Gao, X.; Eila, G. A.; Groß, A.; Passerini, S. Operando pH Measurements Decipher H⁺/Zn²⁺ Intercalation Chemistry in High-Performance Aqueous Zn/δ-V₂O₅ Batteries. *ACS Energy Lett.* **2020**, *5* (9), 2979–2986.

(41) Ma, C. H.; Wang, X.; Lu, W. Q.; Wang, C. Z.; Yue, H. J.; Sun, G.; Zhang, D.; Du, F. Achieving stable Zn metal anode via a simple NiCo layered double hydroxides artificial coating for high performance aqueous Zn-ion batteries. *Chem. Eng. J.* **2022**, *429*, 132576.

(42) Yu, H. M.; Chen, Y. J.; Wei, W. F.; Ji, X. B.; Chen, L. B. A Functional Organic Zinc-Chelate Formation with Nanoscaled Granular Structure Enabling Long-Term and Dendrite-Free Zn Anodes. *ACS Nano* **2022**, *16* (6), 9736–9747.

(43) Ma, C.; Yang, K.; Zhao, S.; Xie, Y.; Liu, C.; Chen, N.; Wang, C.; Wang, D.; Zhang, D.; Shen, Z. X.; et al. Recyclable and Ultrafast Fabrication of Zinc Oxide Interface Layer Enabling Highly Reversible Dendrite-Free Zn Anode. *ACS Energy Lett.* **2023**, *8* (2), 1201–1208.

(44) Guo, Z.; Fan, L.; Zhao, C.; Chen, A.; Liu, N.; Zhang, Y.; Zhang, N. A Dynamic and Self-Adapting Interface Coating for Stable Zn-Metal Anodes. *Adv. Mater.* **2022**, *34* (2), 2105133.

(45) Lin, Y.; Hu, Y.; Zhang, S.; Xu, Z.; Feng, T.; Zhou, H.; Wu, M. Binder-Free Freestanding 3D Zn-Graphene Anode Induced from Commercial Zinc Powders and Graphene Oxide for Zinc Ion Battery with High Utilization Rate. *ACS Appl. Energy Mater.* **2022**, *5* (12), 15222–15232.

(46) Zeng, Y.; Zhang, X.; Qin, R.; Liu, X.; Fang, P.; Zheng, D.; Tong, Y.; Lu, X. Dendrite-Free Zinc Deposition Induced by Multifunctional CNT Frameworks for Stable Flexible Zn-Ion Batteries. *Adv. Mater.* **2019**, *31* (36), 1903675.

(47) Li, H.; Guo, C.; Zhang, T.; Xue, P.; Zhao, R.; Zhou, W.; Li, W.; Elzatahry, A.; Zhao, D.; Chao, D. Hierarchical Confinement Effect with Zincophilic and Spatial Traps Stabilized Zn-Based Aqueous Battery. *Nano Lett.* **2022**, *22* (10), 4223–4231.

(48) Tao, Y.; Zuo, S. W.; Xiao, S. H.; Sun, P. X.; Li, N. W.; Chen, J. S.; Zhang, H. B.; Yu, L. Atomically Dispersed Cu in Zeolitic Imidazolate Framework Nanoflake Array for Dendrite-Free Zn Metal Anode. *Small* **2022**, *18*, No. e2203231.

(49) Ruan, P.; Liang, S.; Lu, B.; Fan, H. J.; Zhou, J. Design Strategies for High-Energy-Density Aqueous Zinc Batteries. *Angew. Chem., Int. Ed.* **2022**, *134* (17), No. e202200598.

(50) Yi, X.; Fu, H.; Rao, A.; Zhang, Y.; Zhou, J.; Wang, C.; Lu, B. Safe electrolyte for long-cycling alkali-ion batteries. *Nat. Sustain.* **2024**, *7*, 326–337.

(51) Geng, Y.; Fu, H.; Hu, Y.; Rao, A. M.; Fan, L.; Zhou, J.; Lu, B. Molecular-level design for a phosphate-based electrolyte for stable potassium-ion batteries. *Appl. Phys. Lett.* **2024**, *124*, 063901.